Journal of
Applied Crystallography
ISSN 0021-8898

Received 15 August 2006
Accepted 29 January 2007

Structural study of nanocrystalline nickel thin films

N. Radic,[a]* P. Dubcek,[a] S. Bernstorff,[b] I. Djerdj[c] and A. M. Tonejc[c]

[a]Rudjer Boskovic Institute, HR-10000, Zagreb, Croatia, [b]Sincrotrone Trieste, I-34012 Basovizza (TS), Italy, and [c]Faculty of Sciences, Department of Physics, HR-10000 Zagreb, Croatia. Correspondence e-mail: radic@irb.hr

Nickel thin films (400 nm) were deposited by magnetron sputtering onto fused silica substrates. The effects of argon pressure and substrate temperature (from room temperature to 973 K) upon the film structure were investigated. The film structure was studied using grazing-incidence small-angle X-ray scattering (GISAXS) and X-ray diffraction (XRD) analysis. It was found that the prepared nanocrystalline Ni films contain two kinds of inhomogeneities observable by GISAXS, namely isotropic and platelet-like. Up to about 373 K the isotropic or spherical 'particles' prevail, while above that temperature the platelet-like 'particles' predominate. These inhomogeneities are ascribed to intergranular matter or grain boundaries, since the grain size (as determined from the XRD patterns) was found to increase from 7 nm in samples deposited at room temperature to about 90 nm in samples deposited at 423 K or higher temperature.

1. Introduction

Nanocrystalline nickel (nc-Ni) is a very interesting material due to its enhanced mechanical (Siow *et al.*, 2004; Yang & Vehoff, 2004), corrosion (Mishra & Balasubramaniam, 2004; Wang *et al.*, 1996) and catalytic (Metikos-Hukovic *et al.*, 2006) properties. Several preparation techniques have been employed so far in order to obtain a bulk material [severe plastic deformation (Zhilyaev *et al.*, 2002, and references therein), ball milling (Bonetti *et al.*, 1999; Valiev *et al.*, 1997) or inert gas condensation followed by compaction of nanocrystalline powders (Birringer *et al.*, 1984)], thick films [direct or pulsed electrodeposition (Shriram *et al.*, 2000; Palumbo *et al.*, 1997; El-Sherik & Erb, 1995)] or thin films [physical vapour deposition methods, PVD (Knapp & Follstaedt, 2004; Zhong *et al.*, 2004; Brunetti & Monticone, 1993; Hugo *et al.*, 2003; Mitra *et al.*, 2001, 2004; Gai *et al.*, 2002; Hurley *et al.*, 2005)]. Among the PVD methods of nc-Ni production, magnetron sputtering has been relatively seldom employed for the preparation of nc-Ni (Brunetti & Monticone, 1993; Hugo *et al.*, 2003; Mitra *et al.*, 2001, 2004; Gai *et al.*, 2002; Hurley *et al.*, 2005). The reason for this might be the fact that nickel is a ferromagnetic material, and thus not very convenient for magnetron sputtering due to its short-circuiting of the magnetic field.

A rather limited range of preparation conditions has been examined in the case of sputter-deposited nc-Ni so far. In Mitra *et al.* (2001), a thorough investigation of the structural properties of nc-Ni thin films prepared at two different substrate temperatures (room temperature and liquid nitrogen temperature, RT and LN, respectively) and with the substrate bias up to −200 V is given. The same preparation conditions were used in Hugo *et al.* (2003), Mitra *et al.* (2001, 2004) and Gai *et al.* (2002).

Here, we present the results of a structural study of nc-Ni films prepared by magnetron sputtering over a wide range of working gas pressure (0.33 to 1.33 Pa) and onto substrates held at temperatures ranging from room temperature to 973 K. The methods of structure investigation were X-ray diffraction (XRD) and grazing-incidence small-angle X-ray scattering (GISAXS).

2. Experimental

Nickel thin films were deposited by magnetron sputtering onto fused silica and single-crystalline Si in the same run. A Torus magnetron designed to sputter magnetic materials was used for nickel sputtering in a CMS18 sputtering system (Kurt J. Lesker Co., Clairton, Pennsylvania, USA). The base pressure in the process chamber was 10^{-6}–10^{-5} Pa, and the working gas was 5 N argon in a continuous flow. The deposition rate was about 7–8 nm min^{-1} at 240–300 W magnetron power, and the final film thickness was about 400 nm. In order to examine the effect on film structure, the argon pressure was varied in the range 0.33–1.33 Pa and the substrate temperature was varied between room temperature and 973 K.

X-ray diffraction patterns of the studied samples were taken at room temperature using a Philips powder diffractometer (PW 1820) with monochromated Cu $K\alpha$ radiation. The structural and microstructural parameters of the investigated Ni thin films were extracted with Rietveld refinement using the program *FULLPROF* (Rodríguez-Carvajal, 2000), employing a modified Thompson–Cox–Hastings pseudo-Voigt (T-C-H pV) (Thompson *et al.*, 1987) as a diffraction profile function. The determination of the volume-weighted average grain sizes (D) and the r.m.s. lattice microstrain ($\langle\varepsilon^2_{hkl}\rangle^{1/2}$) for the Ni films was conducted by line-broadening analysis. The procedure of size–microstrain extraction was performed in the same manner as described elsewhere (Djerdj *et al.*, 2005).

SAXS measurements were performed at the ELETTRA synchrotron radiation source, Trieste (Italy), at the SAXS beamline, using an X-ray beam energy of 8 keV (λ = 1.54 Å). Grazing-incidence measurements were taken at different fixed grazing angles on the sample, using a two-dimensional CCD detector (1024 × 1024 pixels) at a fixed position perpendicular to the incident beam. The spectra were corrected for background intensity and detector response. The incident angle was 0.1° above the critical angle for nickel, which results in about 150 nm X-ray penetration depth.

The atomic force microscopy (AFM) examination of selected samples was performed with the Nanoscope IIIa (Digital Instruments) in a tapping mode.

3. Results

3.1. XRD results

All deposited Ni films were nanocrystalline, with strong preferred orientation along the ⟨111⟩ direction perpendicular to the substrate surface. Fig. 1 shows the 111 Ni peaks for different substrate temperatures. It is clearly visible that, with the increase of the substrate temperature, the line broadening is less pronounced, implying that the crystallites are bigger.

The crystallites grew rapidly from 6.7 nm at RT to as large as 152 nm at 973 K, as seen in Fig. 2. Simultaneously, the lattice microstrain was calculated from the peak broadening. Its average value is around 0.1%, which reflects the presence of lattice imperfections created during the sputtering process.

We also calculated the crystallite size in the other directions, ⟨200⟩ and ⟨220⟩, and we did not find any difference compared with the 111 reflection. This indicates that the line broadening is isotropic (independent of the lattice direction), and consequently it implies that the crystallites are of a spherical shape. The unit-cell parameter a_0 values deduced from the refinement of Ni thin films are shown in Fig. 2 as a function of substrate temperature.

According to the temperature evolution of the lattice parameter, an interesting phenomenon is observed. Going from RT to 673 K, the lattice parameter value decreases from 3.5369 to 3.472 Å. For comparison, the lattice parameter value of Ni given by the International Centre for Diffraction Data (ICDD, Pennsylvania, USA) database is 3.5238 Å (ICDD-PDF No. 4-850). The only exception to this tendency to decrease is the sample deposited at 973 K, where a slight increase of the lattice parameter compared with the previous measuring point (673 K) was observed.

3.2. GISAXS results

Apart from the nanocrystals of different sizes which are present in the nc-Ni films, a considerable fraction of the films (especially of those prepared at lower substrate temperatures) consists of a non-homogenous disordered part mixed with the nanocrystals. In order to study these inhomogeneities we have applied GISAXS to our samples (Amenitsch *et al.*, 1998).

The GISAXS patterns for three samples deposited at different substrate temperatures (RT, 423 K and 573 K) are shown in Fig. 3. Here $q = 4\pi \sin\theta/\lambda$ is the magnitude of scattering vector, where 2θ is the scattering angle and λ is the X-ray wavelength. The z and y components (q_z and q_y, respectively) are in the directions perpendicular to the sample surface, and parallel to the sample surface but perpendicular to the incoming beam, respectively. Basically, the GISAXS patterns consist of two distinct parts whose relative intensity depends on the substrate temperature during deposition. At low temperatures (Fig. 3*a*), isotropic scattering dominates in the GISAXS pattern, while the scattering intensity is anisotropic and elongated along the specular plane at high substrate temperature (Fig. 3*c*). The intermediate substrate temperature (Fig. 3*b*) results in both contributions present at similar intensity levels. In order to follow the changes and evolution of the inhomogeneities with substrate temperature, in Fig. 4 we show the intensities which we extracted from the patterns shown in Fig. 3 along two different directions parallel to the specular plane, *e.g.* at $q_y = 0.075$ Å^{-1} and $q_y = 0.020$ Å^{-1} for a series of substrate temperatures. The chosen cuts were convenient to separate the two distinct contributions to the scattering, since there the isotropic or anisotropic contributions to the scattering are dominant, respectively.

Apart from the Porod (q^{-4}) type scattering above about $q_z = 0.12$ Å^{-1} (coming from the contrast between the disordered part and the larger nanocrystals that are embedded in the film), there is a particle-like scattering at the smaller angles. A simple Guinier approximation was used in order to obtain the radius of gyration (R_G), *e.g.* the typical size of the inhomogeneities as a function of temperature for both contributions to the GISAXS. Corrections for refraction (the bulk density of nickel was used for obtaining the electron density of nc-Ni), absorption and offset from the specular plane were included in the fitting function. Given the restricted angular range due to refraction, the obtained values of R_G serve as a reasonable approximation for the particle sizes and the influence of the sputtering temperature is clearly resolved. The results are presented in Fig. 5. In contrast with the sizes of the nanocrystals, the sizes of the isotropic inhomogeneities fall above 323 K from 8 nm down to 4 nm at 423 K, where this contribution to the scattering fades away. At this temperature, the vertical sizes of the anisotropic inhomogeneities begin to decrease and are down to 3 nm at the highest temperatures (673–973 K), while horizontally they increase up to 14 nm.

The effects of the working gas pressure on the film structure are shown in Fig. 6. It was found that lowering of the pressure results in a

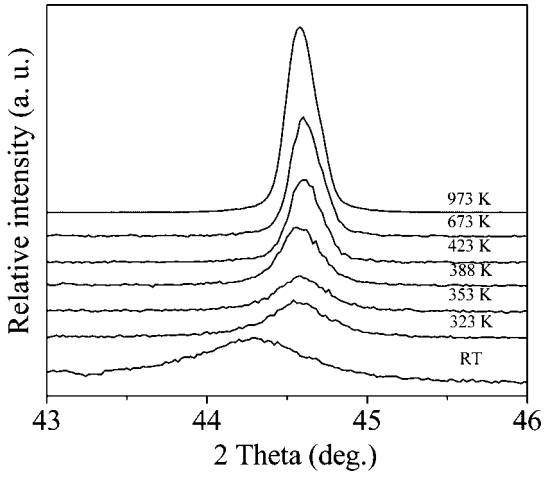

Figure 1
The Ni 111 peak shape as a function of substrate temperature

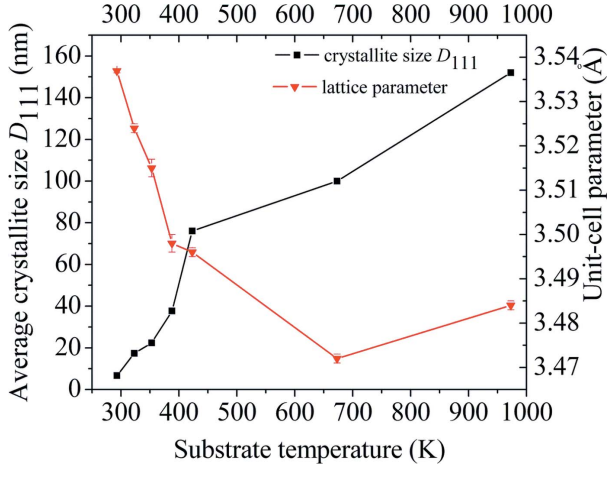

Figure 2
Average grain size of the nc-Ni samples or thin films deposited onto fused silica at different substrate temperatures, and Ni 111 unit-cell parameter variation.

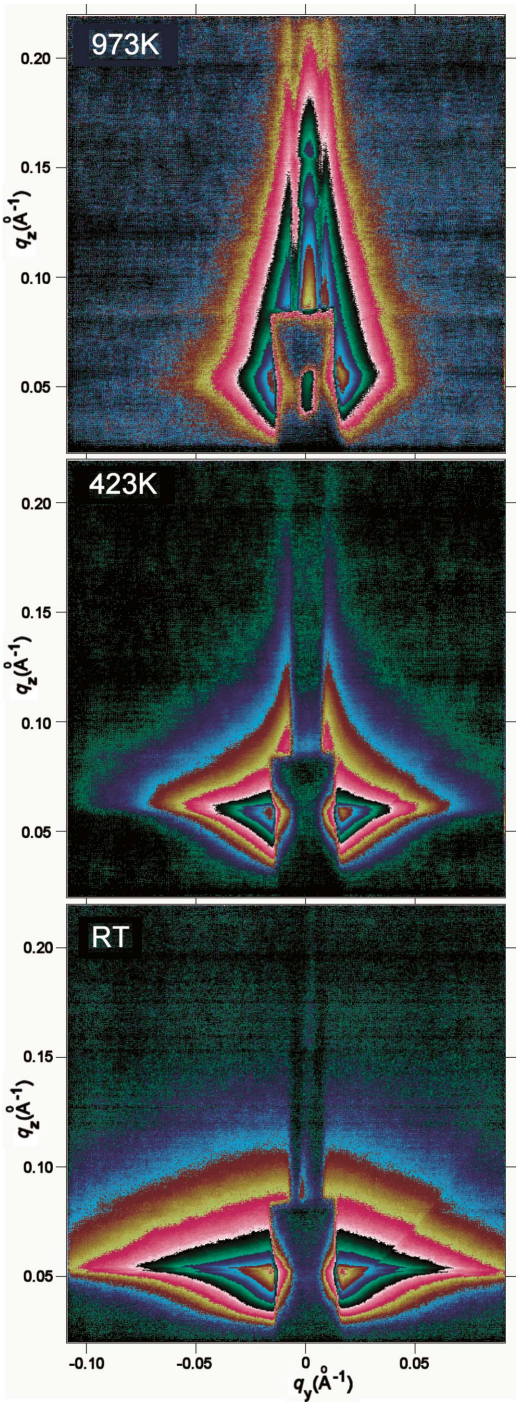

Figure 3
GISAXS patterns taken at 0.7° grazing angle for nc-Ni samples deposited at different substrate temperatures as indicated.

structure equivalent to sputtering at higher substrate temperature. Again, two distinct contributions are present in the GISAXS, similar to those shown in Fig. 3, and using the same procedure explained above we obtained the typical sizes for the inhomogeneities in nc-Ni films sputtered at room temperature, under different argon pressure (Fig. 6). At 0.33 Pa pressure, these sizes are reduced to about 4 nm, which for films deposited at 1.33 Pa pressure was obtained only for films deposited above 423 K.

Finally, we have also examined the topography of the film surface using AFM, in order to establish a correspondence between the XRD

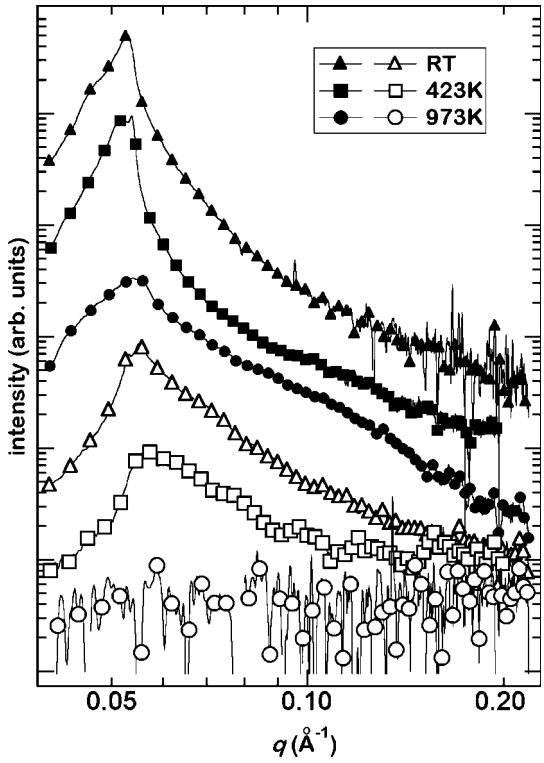

Figure 4
GISAXS intensities along q_y = 0.020 Å^{-1} (full symbols) and q_y = 0.075 Å^{-1} (open symbols) *versus* scattering angle for nc-Ni samples deposited at different substrate temperatures.

size and a direct observation of the surface grain size. The results are shown in Fig. 7 for samples sputtered at room temperature and subsequently isochronally annealed up to 973 K (left and right pictures, respectively). The AFM pictures show a grain-like structure,

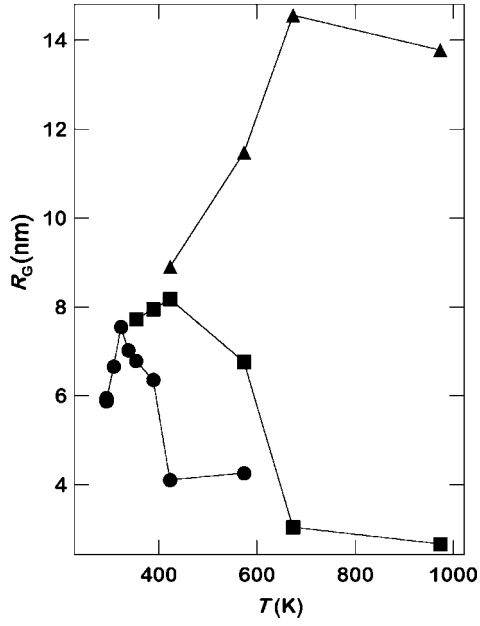

Figure 5
Size of the inhomogeneities in nc-Ni thin films. R_G was derived from GISAXS patterns for two kinds of inhomogeneities or 'particles'. (*a*) Spherical (circles). (*b*) Platelet-like (squares, vertical; triangles, horizontal).

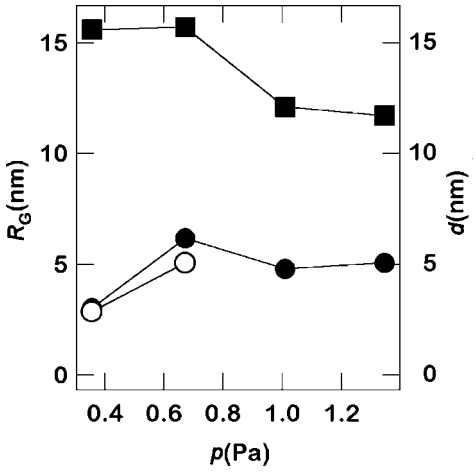

Figure 6
Grain-size d (squares) and R_G (closed and open circles) derived from the XRD and GISAXS patterns, respectively, for two kinds of inhomogeneities or 'particles', (*a*) isotropic (open circles) and (*b*) platelet-like (closed circles) observed in nc-Ni films sputtered under different argon pressure (p).

but the typical sizes are a few times larger than the values obtained by XRD. Apparently, the film growth results in a columnar structure and the grains themselves contain a number of nickel nanocrystals. These are embedded in an amorphous matrix that is inhomogeneous not only in the nanometre size range, but also at this scale.

4. Discussion

The mechanical, electrical, corrosion and catalytic properties of nanocrystalline materials are mostly governed by their microstructure, *i.e.* grain size, primary intercrystalline defects like grain boundaries and triple junctions, secondary defects like porosity, residual amorphous regions, lattice dislocation, vacancies *etc.* Furthermore, the initial structure to a great extent determines the thermal stability of the prepared (metastable) nanocrystalline material. Therefore, insight into the nc-Ni structure is essential for understanding its properties. Only the characteristic results, which include both the grain size and the intercrystalline expanse in nc-Ni samples, are reviewed below.

Severe plastic deformation samples: presumably without contamination and internal porosity, grain size down to about 100 nm, grain boundary thickness presumed to be 0.8–1.0 nm (Zhilyaev *et al.*, 2002, and references therein) or grain boundary width at 10% of the grain radius (10 nm) (Korznikov *et al.*, 2002).

Inert gas condensation followed by compaction: these samples regularly include closed porosities (which might be of the same size as the nanoparticles!), heterogeneities in grain size, and grains which tend to grow upon compaction at elevated temperature. The characteristic grain size is of the order 10–20 nm (Agnew *et al.*, 2000).

Pulsed electrodeposition: a versatile technique which allows several parameters (pulse timing, bath temperature, bath composition *etc.*) to control the nanoparticle size in the range starting from 8–10 nm to several hundreds of nanometres (Aus *et al.*, 1994; Natter *et al.*, 1998, 2001; Kim *et al.*, 2002; Mishra *et al.*, 2004; Da Silva & Klement, 2005). However, impurities from the plating process are unavoidably incorporated into the produced material. The width of the grain boundary is estimated (Aus *et al.*, 1994) to be 1 nm, while the closed porosity volume fraction has been found to decrease from 3% at 17 nm to 1% at 53 nm grain size (Natter *et al.*, 1998).

Finally, nc-Ni films produced by magnetron sputtering have been examined in some detail by XRD, transmission electron microscopy (TEM) and optical microscopy methods (Mitra *et al.*, 2001). It was found that the grain size of nc-Ni deposited at room temperature depends strongly upon substrate bias, increasing from 9 nm at zero bias to 25 nm for a −200 V biased substrate. However, the grain size of a film deposited onto a substrate held at LN temperature is almost independent of the bias applied, and ranges from 11 to 14 nm. Pores were observed but their size not disclosed. A subsequent study of nanoporosity by field emission TEM on similar samples (Gai *et al.*, 2002) revealed pores sized from 1–2 nm along the grain boundaries in RT films, while amorphous Ni-rich regions up to a few nanometres in size were found in the interfacial regions between nanocrystals deposited at LN temperature. nc-Ni films deposited onto NaCl substrates at LN temperature (Hugo *et al.*, 2003) and with a −200 V bias exhibit an average grain size of about 19 nm, with a large number of pores located at grain boundaries. A 772 nm thick nc-Ni film deposited onto Si(001) at RT exhibits an average grain diameter of 27 ± 10 nm, while the average grain size decreases with decreasing

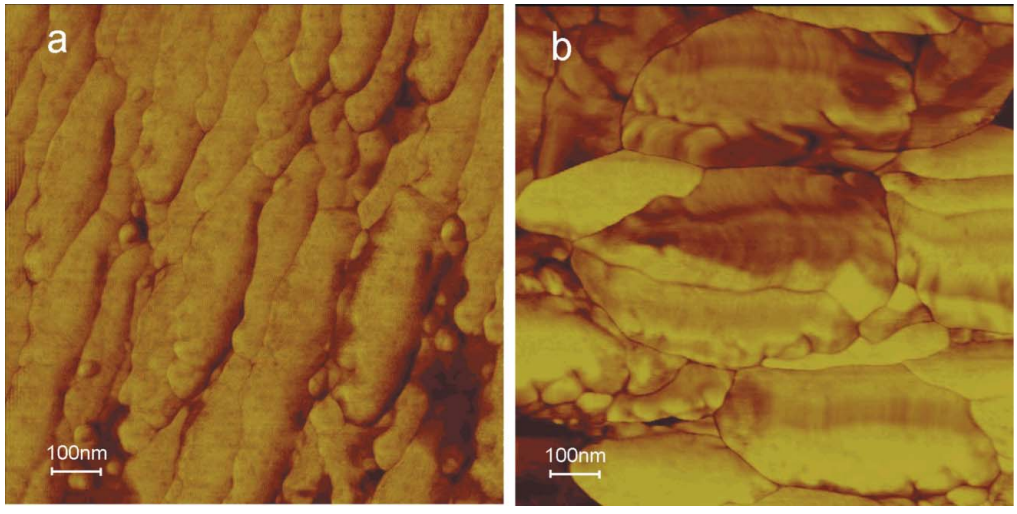

Figure 7
AFM pictures (1 µm × 1 µm) of the nc-Ni samples. (*a*) As-deposited. (*b*) Annealed to 973 K *in vacuo*.

film thickness to 16 ± 6 nm in a 53 nm thick film. From measurements of the elastic mechanical properties of these films, it was assumed that about 11 vol.% is actually occupied by intercrystalline material. It was estimated that the density of the intercrystalline phase is about 82% of the bulk nickel density (8.90 g cm^{-3}), which yields an average density of a nc-Ni film about 1–2% smaller than bulk nickel. The intercrystalline volume fraction increases for thinner films due to the smaller nickel grain sizes. The grain sizes of the actual nc-Ni samples deposited at RT are similar to the values reported by Mitra *et al.* (2001) and thus extend the temperature range examined for the magnetron deposition process up to 973 K.

Our results on the nc-Ni grain size dependence upon argon pressure and substrate temperature can be understood in the framework of deposited Ni atom energy considerations: lower argon pressure allows for a higher average kinetic energy of the depositing Ni atoms. Upon impinging on the surface of the growing film, the Ni atoms dissipate their kinetic energy in several collisions with the atoms of the film. In this random-walk movement along the surface, it is possible to find the site of minimum energy – which is the one in the ordered lattice – to stick at, and thus incorporate into the (nano)-crystal. At higher argon pressure, a low average energy of the depositing atom results in it sticking to the surface at the location where the atom actually landed. Thus, growth of both ordered nanograins and disordered intercrystalline matter are equally probable. The effects of substrate temperature are mostly due to the enhancement of the surface diffusivity of deposited atoms, thus allowing them to find the sites with minimum energy – again the lattice sites of growing grains. Another effect of the substrate temperature might be related to the adsorption isotherms of the residual gases on the growing film surface, which might be incorporated into the intercrystalline matter and stabilize the nanostructure as a whole.

The presented results on intercrystalline matter in nc-Ni films deposited by magnetron sputtering are the first of their kind obtained by GISAXS. It was found that the nc-Ni films contain two kinds of inhomogeneities, isotropic and platelet-like. The isotropic/round particles prevail up to about 373 K, while above that temperature the platelet-like 'particles' predominate. These inhomogeneities are ascribed to intergranular matter or grain boundaries, since the grain size (as determined from the XRD patterns) of the examined sample was found to increase from 12 nm in samples deposited at room temperature to about 90 nm in samples deposited at 423 K or higher temperatures. A tentative explanation for the occurrence of (and competition between) the two kinds of inhomogeneities might be related to the incorporation of residual gases as impurities into the intercrystalline matter. At lower temperatures, the incorporation of adsorbed oxygen might stabilize the isotropic inhomogeneities, which might exhibit an amorphous-like structure (as observed by Brunetti & Monticone, 1993). However, at higher substrate temperatures, the oxygen coverage of the growing film decreases, leading to the formation of 'normal' grain boundaries which are more like platelets of disordered Ni-rich intercrystalline matrix. As regards the characteristic sizes of the observed inhomogeneities, they are somewhat larger than the previously measured or assumed dimensions for intercrystalline matter: 6–8 nm sizes in samples deposited below 573 K are twice as large as the few nanometres estimated for amorphous regions by Gai *et al.* (2002). Only in Natter *et al.* (2001) was the width of the grain boundary region estimated to be equal to 0.1 of the average grain radius, thus about 10 nm. However, if we estimate the volume fraction of the intercrystalline matter (f_{IC}) by taking d from 40 to 90 nm as a characteristic grain size in the 373–573 K range (Fig. 2) in the formula (Natter *et al.*, 1998)

$$f_{IC} = 1 - [(d - \Delta)/d]^3$$

and inhomogeneities of the size Δ = 7 nm, it yields 8–17 vol.%, which is comparable with the results of Hurley *et al.* (2005). As expected, the volume fraction of intercrystalline matter decreases considerably at higher temperatures.

Finally, it should be noted that the change in the ratio between the nanocrystalline and intercrystalline isotropic phases with substrate temperature, as observed by XRD and GISAXS, corresponds well to the variation in electrical resistance of nc-Ni samples deposited at different temperatures, as well as with the hydrogen evolution reaction catalytic activity of nc-Ni films (Metikos-Hukovic *et al.*, 2007).

5. Conclusions

Thin films of nc-Ni have been prepared by magnetron sputtering under various deposition conditions. It was shown that the nc-Ni grain size can be controlled by the working gas pressure and/or by the substrate temperature, yielding grain sizes in the ranges 11–16 nm and 11–150 nm, respectively. GISAXS results reveal that the deposited nc-Ni films contain two distinctive kinds of inhomogeneities, isotropic and platelet-like. The former prevail up to 373 K, and above that temperature the latter are dominant. The 'thickness' of the platelet-like inhomogeneities decreases strongly above 573 K. The observed inhomogeneities are ascribed to intercrystalline matter, since the grain size (as determined from the XRD patterns) of the examined samples was found to increase from 12 nm in samples deposited at room temperature to about 90 nm in samples deposited at 423 K or higher temperature. It is presumed that the occurrence of isotropic inhomogeneities is related to the incorporation of impurities during deposition.

The authors thank Mr. A. Pavlešin for technical assistance. This study was partially funded by the Croatian Ministry of Science, Education and Sports.

References

Agnew, S. R., Elliot, B. R., Youngdahl, C. J., Hemker, K. J. & Weertman, J. R. (2000). *Mater. Sci. Eng. A*, **285**, 391–396.
Amenitsch, H., Rappolt, M., Kriechbaum, M., Mio, H., Laggner, P. & Bernstorff, S. (1998). *J. Synchrotron Rad.* **5**, 506–508.
Aus, M. J., Szpunar, B., Erb, U., El-Sherik, A. M., Palumbo, G. & Aust, K. T. (1994). *J. Appl. Phys.* **75**, 3632–3634.
Birringer, R., Gleiter, H., Klein, H.-P. & Marquardt, P. (1984). *Phys. Lett. A*, **102**, 365–369.
Bonetti, E., Campari, E. G., Pasquini, L., Sampaolesi, E. & Scipione, G. (1999). *Nanostruct. Mater.* **12**, 817–820.
Brunetti, L. & Monticone, E. (1993). *Meas. Sci. Technol.* **4**, 1244–1248.
Da Silva, M. & Klement, U. (2005). *Z. Metallkd.* **96**, 1009–1014.
Djerdj, I., Tonejc, A. M., Tonejc, A. & Radić, N. (2005). *Vacuum*, **80**, 151–158.
El-Sherik, A. M. & Erb, U. (1995). *Plat. Surf. Finish.* **82**, 85–89.
Gai, P. L., Mitra, R. & Weertman, J. R. (2002). *Pure Appl. Chem.* **74**, 1519–1526.
Hugo, R. C., Kung, H., Weertman, J. R., Mitra, R., Knapp, J. A. & Follstaedt, D. M. (2003). *Acta Mater.* **51**, 1937–1943.
Hurley, D. C., Geiss, R. H., Kopycinska-Müller, M., Müller, J., Read, D. T., Wright, J. E., Jennett, N. M. & Maxwell, A. S. (2005). *J. Mater. Res.* **20**, 1186–1193.
Kim, B.-K., Szpunar, J. A. & Varano, R. (2002). *Mater. Sci. Forum*, **408–412**, 937–942.
Knapp, J. A. & Follstaedt, D. M. (2004). *J. Mater. Sci.* **19**, 218–227.
Korznikov, A. V., Pakiela, Z. & Kurzidlowski, K. J. (2002). *Acta Phys. Pol. A*, **102**, 265–271.
Metikos-Hukovic, M., Grubac, Z., Radić, N., Dubcek, P. & Djerdj, I. (2007). *Electrochem. Commun.* **9**, 299–302.
Metikos-Hukovic, M., Grubac, Z., Radić, N. & Tonejc, A. (2006). *J. Mol. Catal. Chem.* **249**, 172–180.

Mishra, R. & Balasubramaniam, R. (2004). *Corros. Sci.* **46**, 3019–3029.
Mishra, R., Basu, B. & Balasubramaniam, R. (2004). *Mater. Sci. Eng. A*, **373**, 370–373.
Mitra, R., Chiou, W. A. & Weertman, J. A. (2004). *J. Mater. Res.* **19**, 1029–1037.
Mitra, R., Hoffman, R. A., Madan, A. & Weertman, J. R. (2001). *J. Mater. Res.* **16**, 1010- 1027.
Natter, H., Löffler, M.-S., Krill, C. E. & Hempelmann, R. (2001). *Scr. Mater.* **44**, 2321–2325.
Natter, H., Schmeltzer, M. & Hempelmann, R. (1998). *J. Mater. Res.* **13**, 1186–1197.
Palumbo, G., Gonzalez, F., Brennenstuhl, A. M., Erb, U., Shmayda, W. & Lichtenberger, P. C. (1997). *Nanostruct. Mater.* **9**, 737–746.
Rodríguez-Carvajal, J. (2000). *FULLPROF*. Program for Rietveld Refinement. Laboratorie Leon Brillouin, CEA-Saclay, France.
Shriram, S., Mohan, S., Renganathan, N. G. & Venkatachalam, R. (2000). *Trans. Inst. Met. Finish.* **78**, 194–197.
Siow, K. S., Tay, A. A. O. & Oruganti, P. (2004). *Mater. Sci. Technol.* **20**, 285–294.
Thompson, P., Cox, D. E. & Hastings, J. B. (1987). *J. Appl. Cryst.* **20**, 79–83.
Valiev, R. Z., Korznikova, G. F., Mulyukov, K. Y., Mishra, R. S. & Mukherjee, A. K. (1997). *Philos. Mag. B*, **75**, 803–811.
Wang, S., Lewis, J. K., Roberge, P. R. & Erb, U. (1996). http://www.corrosionsource.com/events/intercorr/techsess/papers/session4/abstracts/wang.html
Yang, B. & Vehoff, H. (2004). *Z. Metallkd.* **95**, 499–504.
Zhilyaev, A. P., Nurislamova, G. V., Surinach, S., Baro, M. D. & Langdon, T. G. (2002). *Mater. Phys. Mech.* **5**, 23–30.
Zhong, W. H., Sun, C. Q. & Li, S. (2004). *Solid State Commun.* **130**, 603–606.